Digest Journal of Nanomaterials and Biostructures Vol. 16, No. 2, April - June 2021, p. 601 - 612

Fe_3C nanoparticles and carbon nanofiber decorated N-doped carbon framework for bifunctional water splitting

X. E. Gao[a,*], G. Kao[b], J. Yu[b]
[a]*College of Food Engineering, Jilin Engineering Normal University, Changchun, China,130052*
[b]*College of Materials Science and Chemical Engineering, Harbin Engineering University, Harbin, China, 150001*

Transition metal carbides have been widely developed as bifunctional electrocatalysts for water splitting due to their attractive superiority, however, the further environment of their performance still remains a significant challenge. Herein, a novel hierarchical hybrid of Fe_3C nanoparticles and carbon nanofibers supported N-doped carbon framework (Fe_3C@CNF/NC-950 °C) was developed by in situ high-temperature pyrolysis. The introduction of tripolycyanamide induced the formation of carbon nanofibers (CNF), fabricating the hierarchical architecture of 1D CNF and 2D carbon framework. Benefiting from the integration of multicomponent active phases, including Fe_3C nanoparticles, carbon nanofibers and N-doped carbon framework, Fe_3C@CNF/NC-950 °C hybrid electrode presents remarkable electrocatalytic performances toward both hydrogen evolution reaction (HER) and oxygen evolution reaction (OER), as well as robust durability, highlighting Fe_3C@CNF/NC-950 °C as promising alternative of noble-metal-based materials.

(Received February 10, 2021; Accepted May 7, 2021)

Keywords: Iron carbide, Carbon nanofibers, N-doped carbon framework, Hydrogen evolution reaction, Oxygen evolution reaction

1. Introduction

The generation of hydrogen and oxygen with electrocatalytic water splitting is an ideal and environmentally friendly strategy for the development of clean energy, especially hydrogen, which has been considered as a sustainable alternative to traditional fossil fuel due to the high energy density and zero carbon emissions.[1-4] However, high-efficiency electrocatalysts are required in order to accelerate the dissociation of water, involving the cathodic hydrogen evolution reaction (HER) and anodic oxygen evolution reaction (OER).[5-7] Currently, precious metal materials, such as Pt-based materials for HER and Ir/Ru-based materials for OER, exhibit state-of-the-art water electrolysis ability and are recognised as the benchmark electrocatalysts with neutral thermal Gibbs free energy.[8-10] Unfortunately, the single function and high cost circumscribe their industrialization utilization.[11,12] Thus, non-noble-metal materials with superior activity and durability have been widely developed to explore their potential for bifunctional water electrocatalysis.[13-15]

Transition metal carbides (TMCs) attract many attention owing to the ‘‘platinum-like behavior”, as firstly reported by Levy et al[16]. And then remarkable advances have been made

* Corresponding author: gxe@jlenu.edu.cn

based on TMCs, which are highlighted because of some merits, such as noble-metal-like electronic configuration, good conductivity, wide pH reliability, excellent chemical stability along with the corrosion resistance, and also prominent catalytic activity and stability.[17-19] The unique electronic structure characteristics help TMCs to adsorb and activate hydrogen, inducing high intrinsic electrocatalytic ability like Pt. Moreover, TMCs own the interstitial alloy features owing to small carbon atoms located in the interstitial void of densely packed host lattice, forming simple metallic configuration.[20,21] These properties underline TMCs as promising electrocatalysts with innate superiority. For example, Fu et al. prepared the heterogeneous catalyst of V_8C_7 nanomeshs and epitaxial graphene.[22] The exposed active facet, as well as low energy barrier for water dissociation and H intermediate adsorption, contributes jointly to the superior HER performance in both acidic and alkaline conditions. Ye et al. reported cubic iron carbides supported N-doped carbon shell as HER catalyst, requiring an overpotential of 209 mV to afford 10 mA cm^{-2} current density in 1 M KOH.[23] However, the performance of TMCs still needs promotion to the level of precious metal. Efforts have been devoted to designing TMCs-based nanomaterials with high electronic conductivity and well-exposed edge sites, aiming to remarkably reduce the HER and OER overpotentials.[24-26] The integration of 1D and 2D carbon-based nanomaterials has been proved to be a feasible approach to optimize the conductivity at their interface, as well as tune the surface configuration, thus leading to enhanced electrochemical performance in contrast to their single-component counterparts.[27,28]

Inspired by the above concerns, we developed a novel hybrid electrocatalyst based on Fe_3C nanoparticles and carbon nanofibers decorated N-doped carbon framework. High-temperature pyrolysis process results in the fabrication of carbon coated Fe_3C fine nanoparticles, exposing abundant active edge sites. The highly graphitized carbon helps to enhance the intrinsic conductivity of the hybrid. The N-doped hierarchical structure comprised of 1D carbon nanofibers and 2D carbon frameworks would combine the virtues of different dimensional carbonaceous materials.[29] We examined the HER and OER performances of the as-prepared carbides, and found the material obtained at 950 °C (Fe_3C@CNF/NC-950 °C) possessed the most superior electrocatalytic activities and durability. It required the overpotentials of 74.0 and 311.5 mV to deliver 10 mA cm^{-2} current density for HER and OER process, respectively.

2. Experimental section

Preparation of Fe_3C nanoparticles and carbon nanofibers supported N-doped carbon framework: In a typical synthesis process, 0.5 g of Fe $(NO_3)_3 \cdot 9H_2O$, 0.3 g of tripolycyanamide and 1.0 g of polyvinylpyrrolidone (PVP, K30) were mixed to form a 30 mL aqueous solution, which was then placed in a oven at 90 °C until fully dried. The resultant solid was ground and then annealed for 1 h in N_2 atmosphere with the ramp rate of 5 °C min^{-1}. The heat treatment temperatures were set up at 750, 850 and 950 °C, respectively. The corresponding products were defined as Fe_3C@CNF/NC-750 °C, Fe_3C@CNF/NC-850 °C and Fe_3C@CNF/NC-950 °C. The Fe_3C nanoparticles decorated N-doped carbon framework was synthesized similar to Fe_3C@CNF/NC-950 °C except without the addition of tripolycyanamide, named as Fe_3C/NC.

Material characterization: Powder X-ray diffraction (XRD) was performed to analyze the crystalline structure of the as-prepared samples by RigakuTTR-III X-ray diffractometer equipped with a Cu Kα X-ray radiation. The morphology and structure were characterized by scanning electron microscope (SEM, Helios NanoLab G3) and transmission electron microscope (TEM, JEOL JEM-2100). X-ray photoelectron spectroscopy (XPS) was recorded on Escalab250Xi X-ray photoelectron spectrometer.

Electrochemical measurement: The working electrode was prepared by loading the active material on cleaned 1 cm×1 cm Ni foam. Typically, 2 mg of the as-prepared catalysts was

uniformly dispersed into the mixed solution consisted of 480 μL deionized water, 480 μL isopropanol and 40 μL of 5 wt.% Nafion solution, along with the continuous ultrasonic treatment. Then 0.5 mL of the suspension was thoroughly dropped onto the Ni foam electrode. The loading weight of the as-prepared samples on Ni faom is about 1 mg cm^{-2}.

The electrocatalytic HER and OER performances were examined in a traditional three-electrode system based on CHI 760 electrochemical workstation, where the Ni foam loaded catalysts, graphite rod and saturated calomel electrode (SCE) were used as the working, counter and reference electrodes, respectively. N_2 or O_2 saturated 1 M KOH was used as the electrolyte for HER or OER tests, respectively. All related potentials in this work were converted to reversible hydrogen electrode (RHE). The LSV polarization curves were performed at the scan rate of 2 mV s^{-1} and corrected by 95% iR calibrations. Electrochemical impedance spectroscopy (EIS) was observed from the frequency of 100 kHz to 100 mHz with 5 mV AC voltage. The long-term durability was tested by chronopotentiometric measurements and accelerated CV cycles with the scan rate of 100 mV s^{-1}.

3. Results and discussion

The preparation process of Fe_3C nanoparticles and carbon nanofibers supported N-doped carbon framework could be described simply as follows. Iron nitrate, tripolycyanamide and PVP were firstly dispersed to obtain the uniformly mixed powder, which was then directly pyrolyzed by undergoing a high-temperature carbonization procedure.

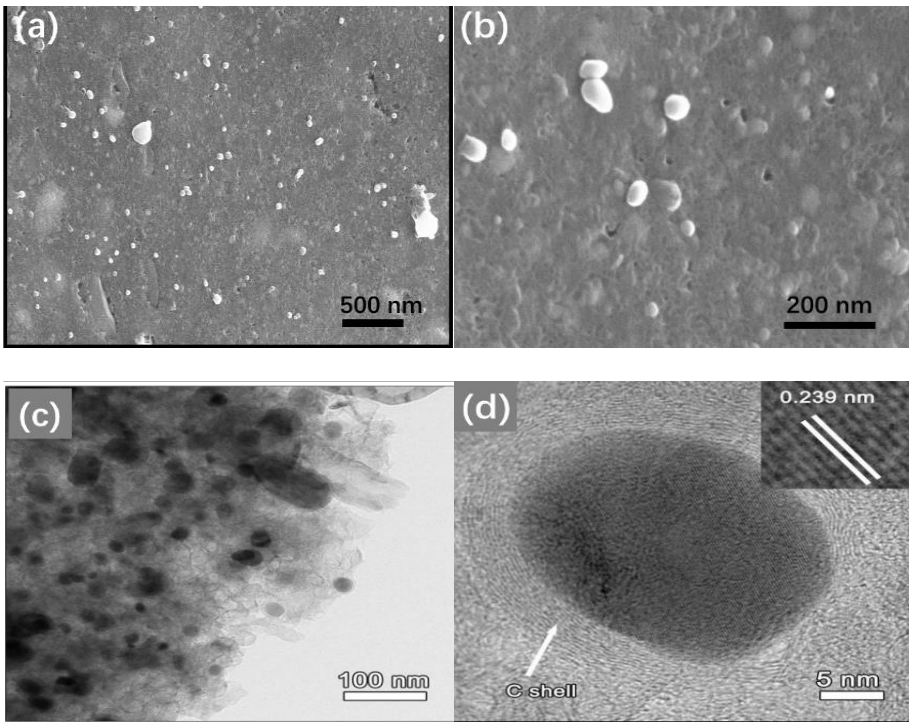

Fig. 1. (a, b) SEM (c) TEM and (d) HRTEM images of Fe_3C/NC.

When the temperature raised above the glass transition temperature, the PVP molten fluid would be destroyed by the tremendous released gas and formed highly open bubble-like structure[30]. Meanwhile, tripolycyanamide was decomposed and transformed into N-doped carbon nanofibers (CNF). Iron nitrate suffered fast decomposition and carbonization to form Fe_3C nanoparticles, generating the strongly coupled Fe_3C core and N-doped carbon shell. Finally, Fe_3C nanoparticles and carbon nanofibers were anchored on N-doped carbon framework. Such porous 3D configuration would be beneficial to the high exposure of active catalytic sites.

Fig. 1 shows the SEM, TEM and HRTEM images of Fe_3C/NC (without the addition of tripolycyanamide). From Figure 1a and 1b, the porous architecture of N-doped carbon substrate was observed along with lots of Fe_3C nanoparticles loaded on the surface. TEM image in Fig. 1c further revealed the highly open structure of carbon framework cross-linked with isolated Fe_3C nanoparticles but there are no carbon nanofibers on the surface. HRTEM image in Figure 1d clearly evidenced that Fe_3C nanoparticles were uniformly coated by graphited carbon shell, which would help to protect inner Fe_3C core from the electrolyte corrosion. The obvious lattice distance of 0.239 nm could be ascribed to the (112) plane of Fe_3C. These results suggest the successful preparation of Fe_3C nanoparticles and decorated N-doped carbon frameworks.

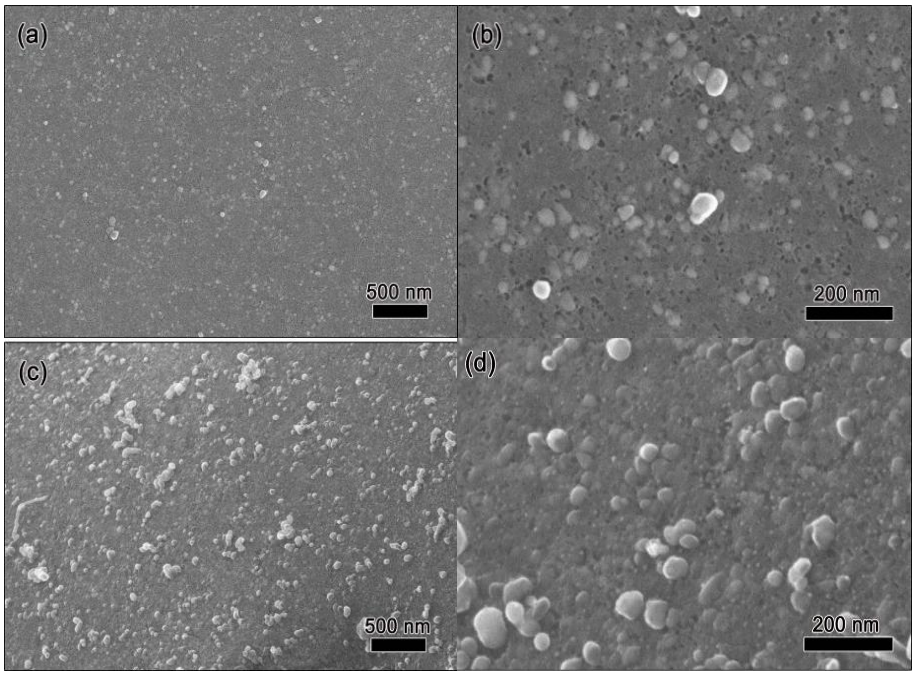

Fig. 2. SEM images of (a, b) Fe_3C@CNF/NC-750 °C, (c, d) Fe3C@CNF/NC-850 °C.

Carbon nanotubes can be obtained on the surface of the samples after the addition of tripolycyanamide and heat treatment. The heat treatment temperatures were set up at 750, 850 and 950 °C, respectively. Fig. 2 shows SEM images of Fe_3C@CNF/NC-750 °C and Fe3C@CNF/NC-850 °C. Similarly, porous architecture of N-doped carbon substrate was observed along with lots of Fe_3C nanoparticles loaded on the surface. Compared Fig. 2a to 2c, by increasing of temperature, carbon nanotubes appear on the surface. And by comparing Figure 2b with 2d, they have similar morphology.

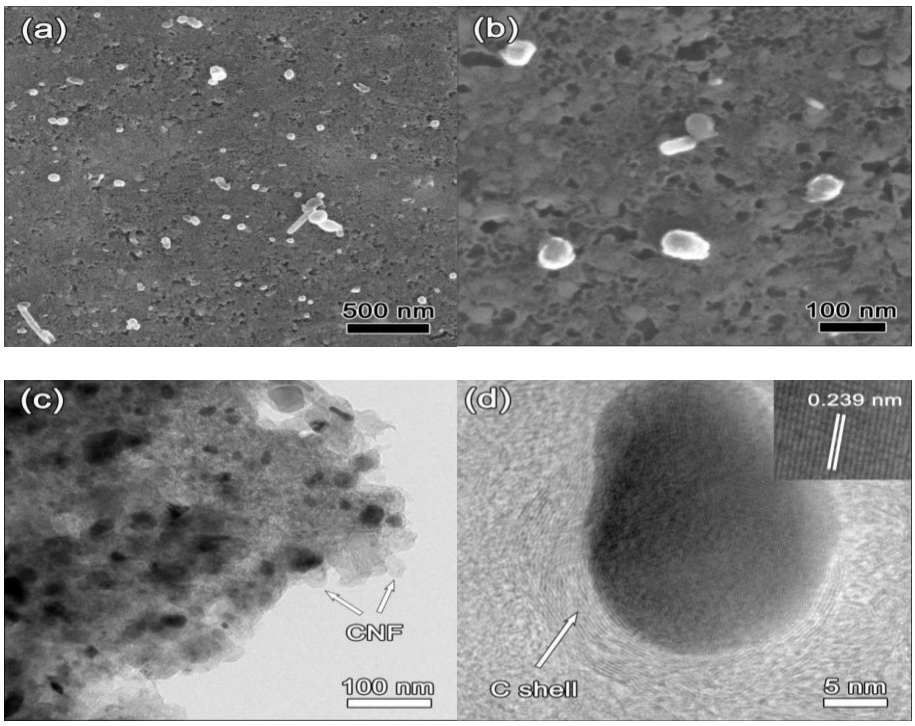

Fig. 3. (a, b) SEM, (c) TEM and (d) HRTEM images of Fe_3C@CNF/NC-950 °C. The arrows in (c) are C nanofibers (CNF) on C framework. The arrow in (d) represents the C shell coated around Fe_3C nanoparticles.

The microstructure of Fe_3C@CNF/NC-950 °C was characterized in detail by SEM and TEM. From Fig. 3a and 3b, the porous architecture of N-doped carbon substrate was observed along with lots of Fe_3C nanoparticles loaded on the surface. And also some carbon nanofibers were exposed and clearly presented. Under an inert atmosphere, the tripolycyanamide precursor with abundant cyanide groups would turn to graphite carbon nitride at a relatively low decomposition temperature (about 400 °C), and then carbon black with the increasing temperature.[31, 32] Due to the existence of Fe species, carbon black would convert to graphite carbon when the annealing temperature surpasses 600 °C.[33] Furtherly, Fe species would play an important role as the growth sites in the formation of carbon nanofibers. TEM image in Fig. 3c further revealed the highly open structure of carbon framework cross-linked with isolated Fe_3C nanoparticles and carbon nanofibers, as marked by the arrows. HRTEM image (Fig. 3d) clearly evidenced that Fe_3C nanoparticles were uniformly coated by graphite carbon shell, which would help to protect inner Fe_3C core from the electrolyte corrosion. The obvious lattice distance of 0.239 nm could be ascribed to the (112) plane of Fe_3C. These results suggest the successful preparation of Fe_3C nanoparticles and carbon nanofibers decorated N-doped carbon frameworks.

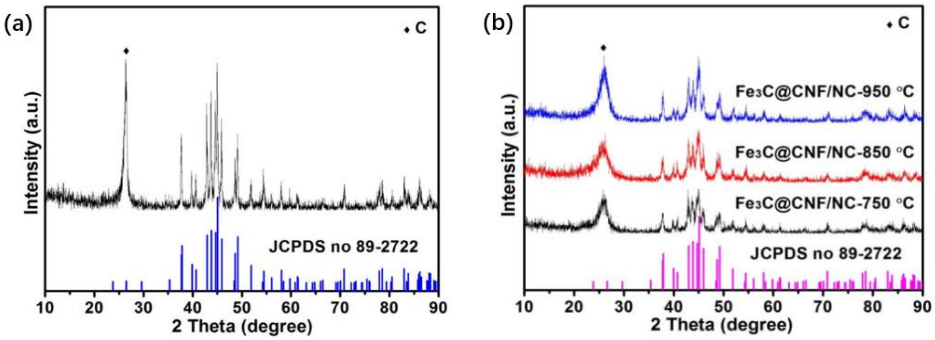

Fig. 4. (a) XRD pattern of Fe_3C/NC. (b) XRD patterns of Fe_3C@CNF/NC obtained at different annealing temperature.

The crystalline features of carbonized materials were investigated by XRD analysis. As showing in Fig. 4a and 4b, the strong peaks positioned at around 26.0°, corresponding to the (002) planes of graphite carbon, indicate the high degree of graphitization. Moreover, the graphitization degree would enhance with the increase of heating treatment temperature. This encourages N-doped carbon framework as the matrix for the electrochemical process owing to high electronic conductivity. Besides, other diffraction peaks match perfectly the characteristics of orthorhombic Fe_3C phase (JCPDS 89-2722), confirming the presence of Fe_3C with high crystallinity.

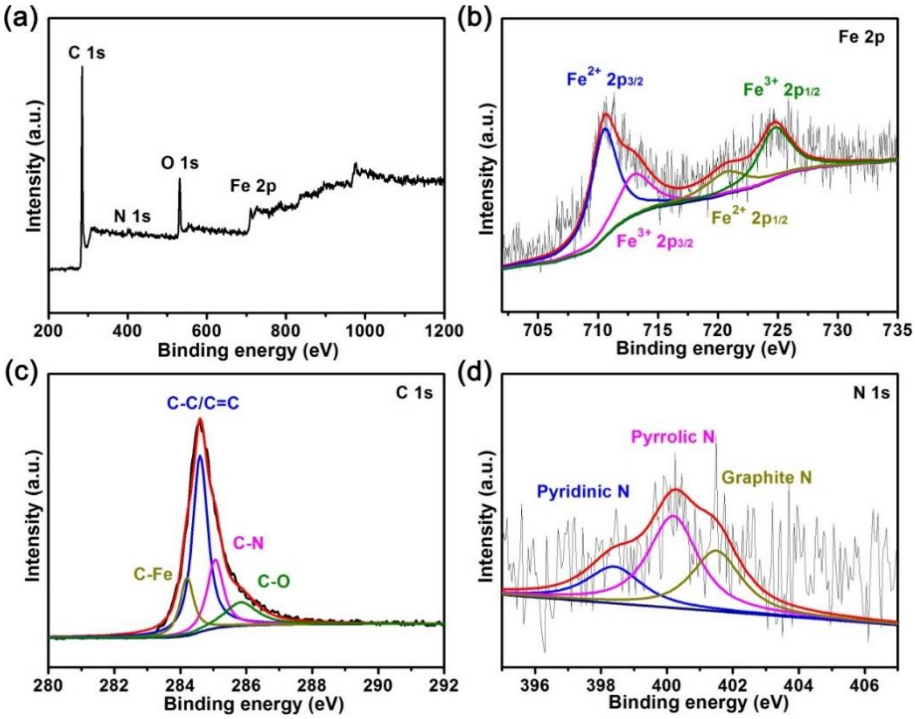

Fig. 5. XPS spectra of Fe_3C@CNF/NC-950 °C. (a) Survey spectrum. High-resolution (b) Fe 2p, (c) C 1s and (d) N 1s spectra.

XPS measurement was performed to reveal the superficial chemical composition and valence states of the as-prepared Fe_3C@CNF/NC-950 °C. The XPS survey spectrum in Fig. 5a suggests the existence of expecting C, N, O and Fe elements. As shown in Fig. 5b, the high-resolution Fe 2p region could be deconvoluted into four peaks, among which the two peaks positioned at 710.5 and 720.7 eV correspond to Fe $2p_{3/2}$ and $2p_{1/2}$ of divalent iron. The signals centered at 713.0 and 724.7 eV are attributed to Fe^{3+} $2p_{3/2}$ and Fe^{3+} $2p_{1/2}$, respectively. This shows the formation of Fe_3C in the composite.[34] With respect to the C 1s spectrum (Figure 5c), the peak is split into four components, located at 284.2, 284.6, 285.1 and 285.8 eV, which could be assigned to C-Fe, C-C, C-N and C-O bonding, respectively. N 1s in Figure 5d fine spectrum reveals the presence of pyridinic N (398.3 eV), pyrrolic N (400.2 eV) and graphitic N (401.4), clearly demonstrating the reservation of N atoms in the carbon architecture.[35] The high content of graphitic N sites enables to facilitate the electronic circulation due to the small atomic radius and strong electronegativity, compared to the original carbon atoms.[36] Thus, high-graphitization carbon frameworks modified by considerable graphitic N may induce positive synergistic interaction with active carbides and enhance their electrocatalytic performances.

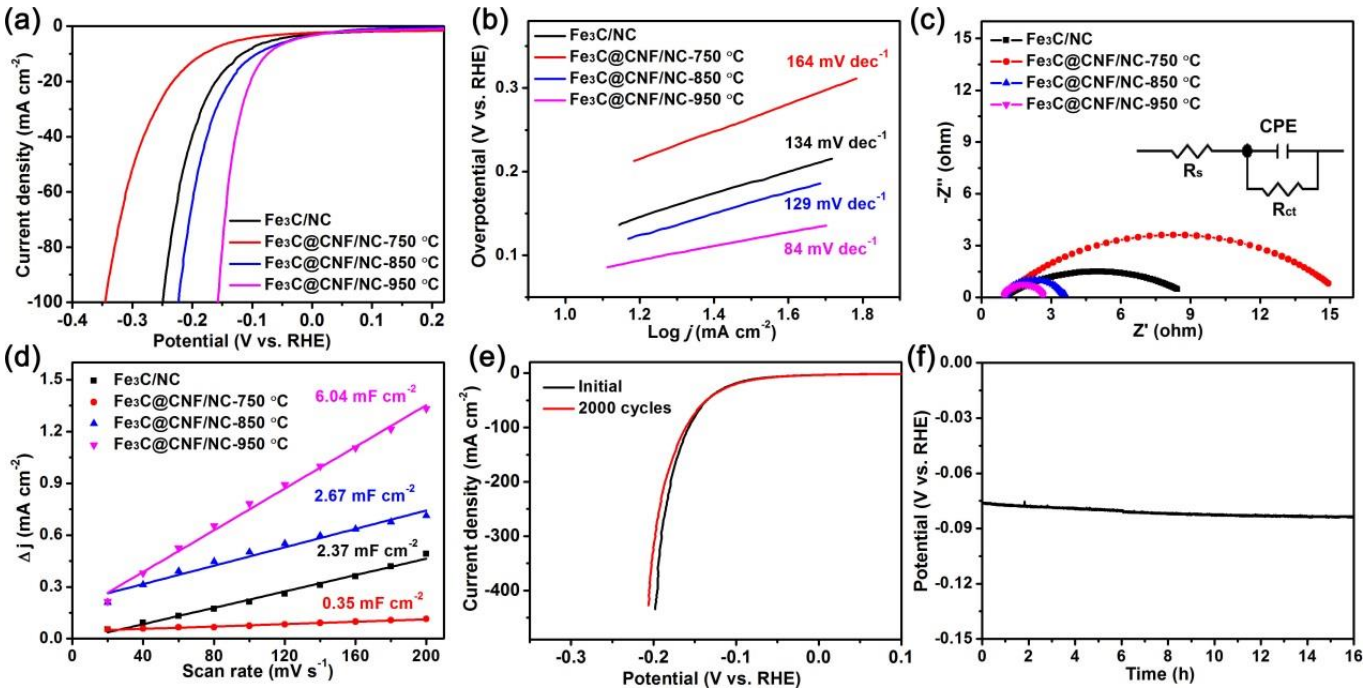

Fig. 6. Electrocatalytic HER performance of the as-prepared samples in 1 M KOH. (a) LSV polarization curves. (b) Corresponding tafel plots. (c) Nyquist plots achieved at the overpotential of 300 mV. (d) Capacitive current as a function of scanning rates. (e) LSV polarization curves of Fe_3C@CNF/NC-950 °C at 1st and 2000 cycles. (f) Chronopotentiometric measurement for 16 h at the current density of 10 mA cm^{-2}.

The electrocatalytic activities of the as-prepared Fe_3C@CNF/NC hybrid electrodes at different annealing temperature were initially assessed in 1 M KOH solution by three-electrode cell. As displayed in Figure 6a, the polarization curve of Fe_3C@CNF/NC-950 °C shows the earliest current response to the cathodic potential. Subsequently, the current density would

dramatically increase with the gradually increasing potential. Fe_3C@CNF/NC-950 °C hybrid electrode needs the overpotential of 74.0 mV to afford 10 mA cm^{-2} current density, which is lower that 116.4 mV for Fe_3C/CNC, 180.5 mV for Fe_3C@CNF/NC-750 °C, and 92.1 mV for Fe_3C@CNF/NC-850 °C, respectively. The HER ability of Fe_3C@CNF/NC-950 °C also exceeds many previously reported carbides in 1 M KOH, such as Ni-Mo_xC/NC-100 (162 mV)[37], V_8C_7 NMs/GR (156 mV)[22], WC-CNTs (137 mV)[38], W-W_2C/CNT (147 mV)[39], Fe_5C_2–Fe_3C@NC (209 mV)[23], Fe-doped Ni_3C (292 mV)[20], $(Fe_{1-x}Dy_x)_3C$/C (381 mV)[40], CoMo carbide@GC (165 mV in 0.1 M KOH)[41], and so on. Meanwhile, the overpotential at 100 mA cm^{-2} for Fe_3C@CNF/NC-950 °C (157.6 mV) is superior to Fe_3C/CNC (249.1 mV), Fe_3C@CNF/NC-750 °C (345.5 mV) and Fe_3C@CNF/NC-850 °C (222.9 mV), indicating outstanding HER activity upon Fe_3C@CNF/NC-950 °C. The HER kinetics of these electrodes were tested by the corresponding Tafel plots exhibited in Figure 6b. The fitted Tafel slope value of Fe_3C@CNF/NC-950 °C is calculated to be 84 mV dec^{-1}, which is smaller that these counterparts, such as 134 mV dec^{-1} for Fe_3C/CNC, 164 mV dec^{-1} for Fe_3C@CNF/NC-750 °C, and 129 mV dec^{-1} for Fe_3C@CNF/NC-850 °C, respectively, revealing the more favorable reaction kinetics based on Fe_3C@CNF/NC-950 °C with the rapidly enhanced current density with the growth of overpotential. The value of 84 mV dec^{-1} is in the range of 40-120 mV dec^{-1}, suggesting the HER process upon Fe_3C@CNF/NC-950 °C obeys a Heyrovsky-dominated Volmer–Heyrovsky mechanism[42,43]. During the hydrogen generation procedure, the reaction undergoes a fast adsorption behavior, and subsequent electrochemical description behavior is thought to be the reaction-controlling step.[44]

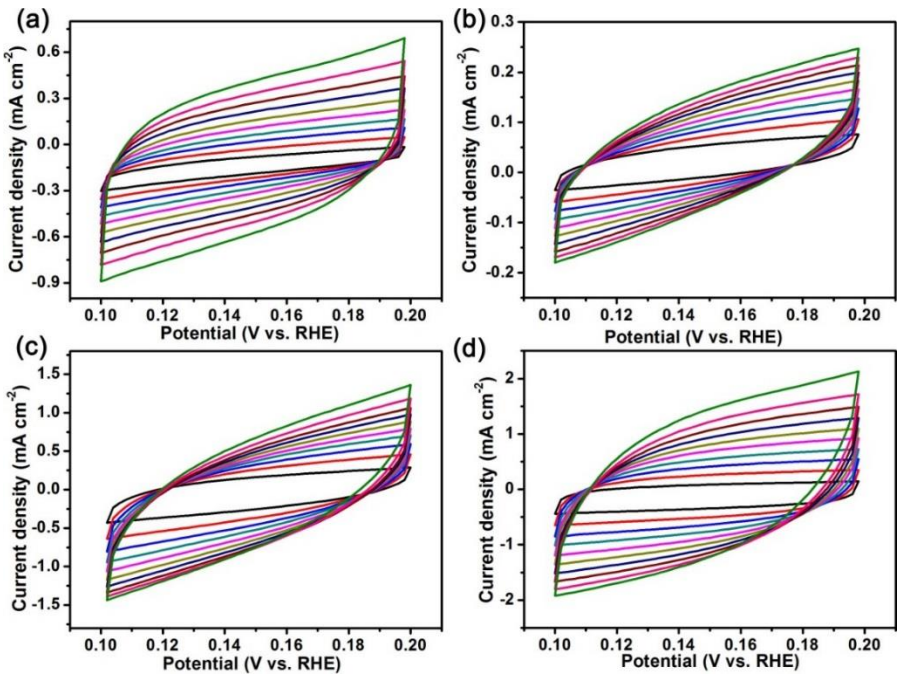

Fig. 7. CV curves of (a) Fe_3C/NC, (b) Fe_3C@CNF/NC-750 °C, (c) Fe_3C@CNF/NC-850 °C and (d) Fe_3C@CNF/NC-950 °C at different scan rates from 20 to 200 mV s^{-1}.

Furthermore, the electrode reaction kinetics and interface characteristics toward HER process were studied by electrochemical impedance spectra (EIS). The Nyquist plots in Fig. 6c reveals Fe_3C@CNF/NC-950 °C possesses the smallest semicircle diameter, whose R_{ct} value is calculated to be 1.7 Ω, much lower than that of Fe_3C/NC (8.1 Ω), Fe_3C@CNF/NC-750 °C (14.7 Ω) and Fe_3C@CNF/NC-850 °C (2.5 Ω). This confirms that Fe_3C@CNF/NC-950 °C possesses the smallest charge-transfer resistance along with the most favorable charge transfer dynamics for hydrogen evolution. In order to clarify the active role of Fe_3C, CNF, N-doped carbon and their synergistic interaction, electrochemical active surface area (ECSA) of the as-prepared samples was investigated via electrochemical double-layer capacitance (C_{dl}) obtained by the CV curves at different scan rates.[45] According to the previous report, the ECSA is proportional to the C_{dl} value for similar materials tested in an identical solution.[46] As shown in Fig. 6d, Fe_3C@CNF/NC-950 °C owns the largest C_{dl} value of 6.04 mF cm^{-2} among a set of the as-prepared Fe_3C catalysts, including Fe_3C/NC (2.37 mF cm^{-2}), Fe_3C@CNF/NC-750 °C (0.35 mF cm^{-2}) and Fe_3C@CNF/NC-850 °C (2.67 mF cm^{-2}). Therefore, it is reasonable to claim Fe_3C@CNF/NC-950 °C possesses the largest ECSA, enabling to expose abundant access inherent active sites. Thus promoting the electrochemical reaction. Apart from the superior catalytic activity, durability of the electrocatalyst is also a key indicator to evaluate the performance of materials. As shown in Fig. 7, stability of Fe_3C@CNF/NC-950 °C for HER was first checked by the continuous and accelerated CV scanning. The polarization curve after 2000 CV cycles present the similar trend to the original curve, along with the negligible cathodic current degeneration. Furthermore, the chronopotentiometric result indicates that no noticeable potential change is observed with 16 h of continuous operation, suggesting the excellent stability of Fe_3C@CNF/NC-950 °C.

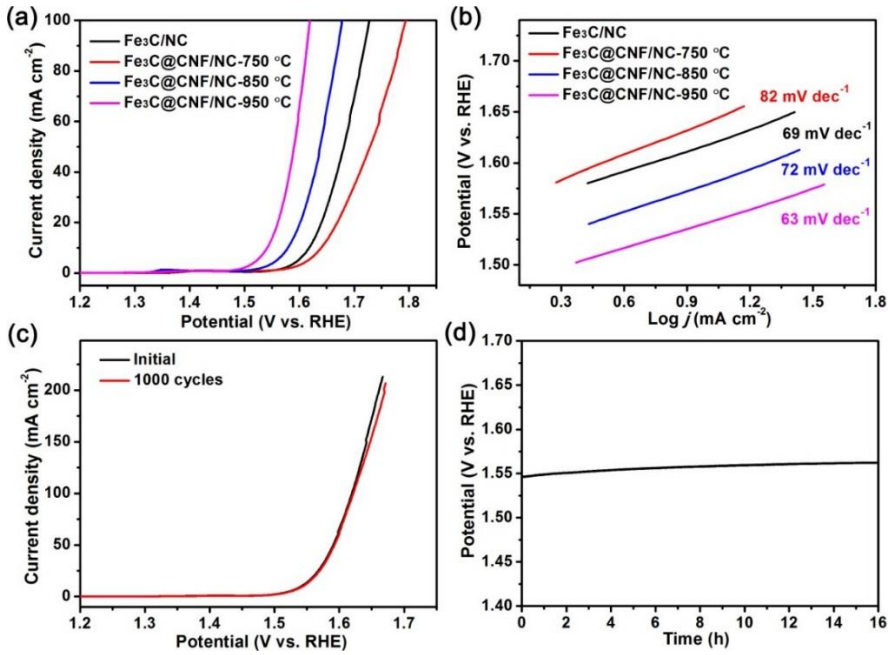

Fig. 8. Electrocatalytic OER performance of the as-prepared samples in 1 M KOH. (a) LSV polarization curves. (b) Corresponding tafel plots. (c) LSV polarization curves of Fe_3C@CNF/NC-950 °C at 1st and 1000 cycles. (f) Chronopotentiometric measurement for 16 h at the current density of 10 mA cm^{-2}.

The OER performance of Fe_3C@CNF/NC-950 °C is also assessed in identical electrolyte to HER to explore its bifunctional potential. As presented in Figure 8a, the LSV curves reveal that a 10 mA cm^{-2} current density could be realized at a low overpotential of 311.5 mV, much lower than that of Fe_3C/NC (388.1 mV), Fe_3C@CNF/NC-750 °C (409.9 mV) and Fe_3C@CNF/NC-850 °C (349.5 mV). We also compare the overpotentials at high current density of 100 mA cm^{-2}, which are 389.1, 496.9, 564.3 and 446.8 mV for Fe_3C@CNF/NC-950 °C, Fe_3C/NC, Fe_3C@CNF/NC-750 °C and Fe_3C@CNF/NC-850 °C, respectively, demonstrating the outstanding OER activity based Fe_3C@CNF/NC-950 °C hybrid electrode. The corresponding tafel slope of Fe_3C@CNF/NC-950 °C is estimated to be 63 mV dec^{-1}, which is also the smallest among these catalysts, indicating the most advantageous oxygen evolution kinetics. Of note, the polarization curve of Fe_3C@CNF/NC-950 °C at 2000 CV cycles only illustrates weak delay of anode current density. No obvious performance regression is observed in the long-term chronopotentiometric measurement. These results encourage Fe_3C@CNF/NC-950 °C as attractive OER electrocatalyst with superior activity and robust stability.

On the basis of the aforementioned analysis, we attribute the bisectional excellent catalytic performances of Fe_3C@CNF/NC-950 °C the following aspects. The small particle sizes of Fe_3C nanoparticles endow them with the large surface area, and help to expose and fully utilize active edge sites. Meanwhile, Fe_3C nanoparticles is encapsulated with N-doped carbon, beneficial to prevent the long-time correction of active Fe_3C from the alkaline electrolyte. Porous N-doped carbon frameworks provide relatively open channels for convenient electrolyte diffusion and charge transfer. The high annealing temperature induces the generation of highly graphited carbon, which also acts as the highly conductive matrix to load active Fe_3C material. Moreover, the formation of carbon nanofibers would further increase the surface area of hybrid. Thus, the main reason for the high-performance and bifunctional electrocatalytic ability lies in the integration of multicomponent active phases including Fe_3C, CNF and N-doped carbon, encouraging Fe_3C@CNF/NC-950 °C to be prospective alternative of noble-metal-based materials.

4. Conclusions

In summary, we reported the in situ pyrolysis synthesis of Fe_3C nanoparticles and carbon nanofibers decorated N-doped carbon framework, which was employed as the potential electrocatalyst for bifunctional water splitting. Unique structural features endow Fe_3C@CNF/NC-950 °C hybrid with high electronic conductivity and abundant active sites. The as-prepared hybrid electrode exhibits superior HER and OER performances with the low overpotentials of 74.0 and 311.5 mV to realize 10 mA cm^{-2}, as well as robust long-term stability. This work may serve as a strategy to rationally design and fabricate hybrid electrode materials for high-performance water splitting.

Acknowledgments

This work was supported by the 13th Five-Year Plan science and technology projects in Jilin Province Department of Education (JJKH20200183KJ).

References

[1] Y. Shi, B. Zhang, Chem. Soc. Rev. **45**, 1529 (2016).

[2] X. Yu, Z.-Y. Yu, X.-L. Zhang, Y.-R. Zheng, Y. Duan, Q. Gao, R. Wu, B. Sun, M.-R. Gao, G. Wang, S.-H. Yu, J. Am. Chem. Soc. **141**, 7537 (2019).

[3] B. Zhu, R. Zou, Q. Xu, Adv. Energy Mater. **8**, 1801193 (2018).

[4] X. L. Wang, W. Feng, X. G. An, C. Lu, W. J. Bai, F. Y. Sun, Q. Q. Kong, Dig. J. Nanomater. Bios. **4**, 1197 (2020).

[5] H. Yan, Y. Xie, A. Wu, Z. Cai, L. Wang, C. Tian, X. Zhang, H. Fu, Adv. Mater. **31**, 1901174 (2019).

[6] J. Yu, Q. Li, Y. Li, C.-Y. Xu, L. Zhen, V. P. Dravid, J. Wu, Adv. Funct. Mater. **26**, 7644 (2016).

[7] C. Zequine, S. Bhoyate, F. Wang, X. Li, K. Siam, P. K. Kahol, R. K. Gupta, J. Alloy. Compd. **784**, 1 (2019).

[8] H. Yan, C. Tian, L. Wang, A. Wu, M. Meng, L. Zhao, H. Fu, Angew. Chem. Int. Ed. **54**, 6325 (2015).

[9] Y. Jiao, Y. Zheng, M. Jaroniec, S. Z. Qiao, Chem. Soc. Rev. **44**, 2060 (2015).

[10] C. Tang, L. Gan, R. Zhang, W. Lu, X. Jiang, A. M. Asiri, X. Sun, J. Wang, L. Chen, Nano Lett. **16**, 6617 (2016).

[11] Y. Zhang, L. Gao, E.J.M. Hensen, J. P. Hofmann, ACS Energy Lett. **3**, 1360 (2018).

[12] C. Guan, W. Xiao, H. Wu, X. Liu, W. Zang, H. Zhang, J. Ding, Y. P. Feng, S. J. Pennycook, J. Wang, Nano Energy **48**, 73 (2018).

[13] Y. Gu, S. Chen, J. Ren, Y. A. Jia, C. Chen, S. Komarneni, D. Yang, X. Yao, ACS Nano **12**, 245 (2018).

[14] F. Yu, H. Zhou, Y. Huang, J. Sun, F. Qin, J. Bao, W. A. Goddard, S. Chen, Z. Ren, Nat. Commun. **9**, 2551 (2018).

[15] X. Wang, W. Ma, C. Ding, Z. Xu, H. Wang, X. Zong, C. Li, ACS Catal. **8**, 9926 (2018).

[16] R. B. Levy, M. Boudart, Science **181**, 547 (1973).

[17] H. Yan, Y. Xie, Y. Jiao, A. Wu, C. Tian, X. Zhang, L. Wang, H. Fu, Adv. Mater. **30**, 1704156 (2018).

[18] Q. Gao, W. Zhang, Z. Shi, L. Yang, Y. Tang, Adv. Mater. **31**, 1802880 (2019).

[19] X. Ma, K. Li, X. Zhang, B. Wei, H. Yang, L. Liu, M. Zhang, X. Zhang, Y. Chen, J. Mater. Chem. A **7**, 14904 (2019).

[20] H. Fan, H. Yu, Y. Zhang, Y. Zheng, Y. Luo, Z. Dai, B. Li, Y. Zong, Q. Yan, Angew. Chem. Int. Ed. **56**, 12566 (2017).

[21] Y. Xie, M. Naguib, V. N. Mochalin, M. W. Barsoum, Y. Gogotsi, X. Yu, K.-W. Nam, X.-Q. Yang, A. I. Kolesnikov, P. R. C. Kent, J. Am. Chem. Soc. **136**, 6385 (2014).

[22] W. Fu, Y. Wang, H. Zhang, M. He, L. Fang, X. Yang, Z. Huang, J. Li, X. Gu, Y. Wang, J. Catal. **369**, 47 (2019).

[23] Z. Ye, Y. Qie, Z. Fan, Y. Liu, Z. Shi, H. Yang, Dalton Trans. **48**, 4636 (2019).

[24] M. Miao, J. Pan, T. He, Y. Yan, B.Y. Xia, X. Wang, Chem.-Eur. J. **23**, 10947 (2017).

[25] C. He, T. Bo, B. Wang, J. Tao, Nano Energy **62**, 85 (2019).

[26] G. Liu, H. Bai, Y. Ji, L. Wang, Y. Wen, H. Lin, L. Zheng, Y. Li, B. Zhang, H. Peng, J. Mater. Chem. A **7**, 12434 (2019).

[27] Y. Li, F. Cheng, J. Zhang, Z. Chen, Q. Xu, S. Guo, Small **12**, 2839 (2016).

[28] Z. Chen, R. Wu, Y. Liu, Y. Ha, Y. Guo, D. Sun, M. Liu, F. Fang, Adv. Mater. **30**,

1802011 (2018).
[29] Z.-Y. Wu, X.-X. Xu, B.-C. Hu, H.-W. Liang, Y. Lin, L.-F. Chen, S.-H. Yu, Angew. Chem. Int. Ed. **54**, 8179 (2015).
[30] Y. Dong, M. Yu, Z. Wang, Y. Liu, X. Wang, Z. Zhao, J. Qiu, Adv. Funct. Mater. **26**, 7590 (2016).
[31] Y. Lai, Y. Jiao, J. Song, K. Zhang, J. Li, Z. Zhang, Materials Chemistry Frontiers **2**, 376 (2018).
[32] Y. Li, B. Jia, Y. Fan, K. Zhu, G. Li, C.-Y. Su, Adv. Energy Mater. **8**, 1702048 (2018).

[33] W. Ma, N. Wang, Y. Du, T. Tong, L. Zhang, K.-Y. Andrew Lin, X. Han, Chem. Eng. J. **356**, 1022 (2019).
[34] N. Song, F. Ma, Y. Zhu, S. Chen, C. Wang, X. Lu, ACS Sustainable Chem. Eng. **6**, 16766 (2018).
[35] H. Jiang, Y. Yao, Y. Zhu, Y. Liu, Y. Su, X. Yang, C. Li, ACS Appl. Mater. Interfaces **7**, 21511 (2015).
[36] X. Duan, K. O'Donnell, H. Sun, Y. Wang, S. Wang, Small **11**, 3036 (2015).
[37] D. Das, S. Santra, K. K. Nanda, ACS Appl. Mater. Interfaces **10**, 35025 (2018).
[38] X. Fan, H. Zhou, X. Guo, ACS Nano 9 (2015) 5125-5134.
[39] Y. Hu, B. Yu, M. Ramadoss, W. Li, D. Yang, B. Wang, Y. Chen, ACS Sustainable Chem. Eng. **7**, 10016 (2019).
[40] Z. Ye, X. Lei, N. Zhao, Y. Qie, X. Yang, Z. Shi, H. Yang, Ceram. Int. **44**, 15256 (2018).
[41] X. Zhao, X. He, F. Yin, B. Chen, G. Li, H. Yin, Int. J. Hydrog. Energy **43**, 22243 (2018).
[42] J. Yu, W.-J. Li, H. Zhang, F. Zhou, R. Li, C.-Y. Xu, L. Zhou, H. Zhong, J. Wang, Nano Energy **57**, 222 (2019).
[43] J.-T. Ren, L. Chen, G.-G. Yuan, C.-C. Weng, Z.-Y. Yuan, Electrochim. Acta **295**, 148 (2019).
[44] J. Yu, Y. Tian, F. Zhou, M. Zhang, R. Chen, Q. Liu, J. Liu, C.-Y. Xu, J. Wang, J. Mater. Chem. A **6**, 17353 (2018).
[45] C. C. Yang, S. F. Zai, Y. T. Zhou, L. Du, Q. Jiang, Adv. Funct. Mater. **0**, 1901949 (2019).
[46] H. Deng, C. Zhang, Y. Xie, T. Tumlin, L. Giri, S.P. Karna, J. LinJ. Mater. Chem. A **4**, 6824 (2016).